Nanoscale

PAPER

View Article Online
View Journal

Cite this: DOI: 10.1039/c9nr04981a

Quantifying the effects of engineered nanomaterials on endothelial cell architecture and vascular barrier integrity using a cell pair model†

Feyisayo Eweje, ‡[a] Herdeline Ann M. Ardoña, ‡[a] John F. Zimmerman, [a] Blakely B. O'Connor, [a] Seungkuk Ahn,[a] Thomas Grevesse,§[a] Karla N. Rivera,[a] Dimitrios Bitounis, [b] Philip Demokritou[b] and Kevin Kit Parker *[a]

Engineered nanomaterials (ENMs) are increasingly used in consumer products due to their unique physicochemical properties, but the specific hazards they pose to the structural and functional integrity of endothelial barriers remain elusive. When assessing the effects of ENMs on vascular barrier function, endothelial cell monolayers are commonly used as *in vitro* models. Monolayer models, however, do not offer a granular understanding of how the structure–function relationships between endothelial cells and tissues are disrupted due to ENM exposure. To address this issue, we developed a micropatterned endothelial cell pair model to quantitatively evaluate the effects of 10 ENMs (8 metal/metal oxides and 2 organic ENMs) on multiple cellular parameters and determine how these parameters correlate to changes in vascular barrier function. This minimalistic approach showed concerted changes in endothelial cell morphology, intercellular junction formation, and cytoskeletal organization due to ENM exposure, which were then quantified and compared to unexposed pairs using a "similarity scoring" method. Using the cell pair model, this study revealed dose-dependent changes in actin organization and adherens junction formation following exposure to representative ENMs (Ag, TiO_2 and cellulose nanocrystals), which exhibited trends that correlate with changes in tissue permeability measured using an endothelial monolayer assay. Together, these results demonstrate that we can quantitatively evaluate changes in endothelial architecture emergent from nucleo-cytoskeletal network remodeling using micropatterned cell pairs. The endothelial pair model therefore presents potential applicability as a standardized assay for systematically screening ENMs and other test agents for their cellular-level structural effects on vascular barriers.

Received 11th June 2019,
Accepted 13th September 2019

DOI: 10.1039/c9nr04981a

rsc.li/nanoscale

Introduction

The vascular endothelium is a selective biological barrier that regulates the exchange of proteins, fluids, and solutes between the intravascular fluid and surrounding vascularized tissues. When damaged due to inflammatory agents, pathogens, or tissue injury, vascular endothelial tissues can become dysfunctional and potentiate unnecessary interstitial fluid accumulation, impaired tissue perfusion, and plasma protein leakage *via* paracellular pathways.[1] Together, these events induce pathophysiological processes that contribute to organ dysfunction in many disease states—most notably sepsis and septic shock.[2] Engineered nanomaterials (ENMs), though increasingly incorporated into a variety of consumer products due to their unique physiochemical properties,[3] have been reported to cause negative effects on the barrier function of the vascular endothelium.[4–6] Particularly, several ENMs were shown to induce changes in endothelial cell morphology, intercellular junction formation, and cytoskeletal protein organization with negative ramifications on endothelial barrier function.[7–12] In such studies, tissue monolayers are commonly used as *in vitro* endothelial models for assessing the effects of ENMs on vascular barrier structure and function. Although changes in cellular-level features could lend important mechanistic insights into ENM toxicities, monolayer models are typically used for monitoring tissue-level function and are often not amenable for systematically measuring alterations in cellular structure

[a]*Disease Biophysics Group, Wyss Institute for Biologically Inspired Engineering, John A. Paulson School of Engineering and Applied Sciences, Harvard University, Cambridge, MA 02138, USA. E-mail: kkparker@seas.harvard.edu*
[b]*Center for Nanotechnology and Nanotoxicology, Department of Environmental Health, T. H. Chan School of Public Health, Harvard University, Boston, MA 02115, USA*

†Electronic supplementary information (ESI) available. See DOI: 10.1039/c9nr04981a

‡These authors contributed equally.

§Present Address: Department of Biology, Concordia University, Montréal, QCH3G 1 M8, Canada

during nanomaterial exposure. The indeterminate cell size, shape, and orientation within endothelial monolayers make it difficult to quantitatively analyze how ENMs may impact subcellular structures, especially at lower doses of exposure.

Since the emergence of biological applications of soft lithography,[13–15] micropatterned multicellular assemblies have been considered a promising alternative model for systematically evaluating morphological changes of cells or tissues in response to a plethora of external stimuli.[16,17] Substrates with micropatterned proteins control the geometry of cells with sub-micron resolution and thus recapitulate important aspects of the *in vivo* microenvironment by dictating limits on cell architecture, adhesion, and spreading reminiscent of those imposed by the extracellular matrix (ECM) and neighboring cells in the body.[16,18,19] Protein micropatterning has also been used for generating isolated cell pairs (*i.e.*, two cells sharing one edge) to study epithelial cell–cell adhesion, junction organization, and stability,[20–22] as well as to investigate cardiomyocyte electrical and structural coupling,[23–25] cellular self-organization,[26] and contact-mediated keratinocyte differentiation.[27] Cell pairs effectively serve as the smallest functional repeating unit of a continuous tissue, which are useful for modeling junction-dependent cell interactions that occur in physiological tissue barriers. The confinement of cell pairs within specific protein micropatterns therefore presents a way to systematically evaluate the effects of different nanoparticle test agents on barrier tissues at a more local spatial scale.

In this study, we hypothesize that micropatterned endothelial cell pairs with defined geometries and junction orientation can serve as a reductionist model for revealing how certain ENMs induce concerted changes amongst structural features of vascular endothelial cells. Because ECM protein micropatterns drive a reproducible cell pair shape and arrangement, this model enables a systematic and quantitative analysis of changes in cellular-level structural parameters that can be used as indicators of degrading barrier function. Here, structural changes in endothelial cell pairs were measured following exposure to 10 different ENMs commonly used for commercial or research purposes (Au, Ag, TiO_2, ZnO, SiO_2, CuO, Fe_2O_3, Al_2O_3 and 2 nanocellulose forms). Adherens junction protein expression and intercellular gap formation, which are commonly correlated to the degree of paracellular permeability across endothelial cells, were among the parameters measured using the pair model. In an effort to further investigate how the impact of various ENMs on tissue barrier function are reflected in the overall cellular structure, we also evaluated key cell architectural features such as cell morphology, cytoskeletal reorganization (*e.g.*, transition from predominantly cortical actin to stress fiber formation, changes in focal adhesion distribution) and nuclear morphology. Additionally, the cell pair model serves as a probe for understanding how such cellular features change due to the perturbation of cell–cell and cell–ECM interactions upon exposure to ENMs. The summative ENM-induced changes in these endothelial structural features were then assessed for their correspondence to effects on cellular viability and tissue-level barrier function. The analyses described here will focus on decreasing endothelial barrier function due to structural integrity degradation (*i.e.*, increased permeability) rather than barrier blockage by external agents. Overall, endothelial cell pairs are demonstrated here as a reductionist model for: (i) quantifying the cellular-level effects of selected ENMs on endothelial barriers; (ii) identifying the doses at which those ENMs start to strucally impact the cells; and (iii) establishing whether such structural changes in cells correlate to functional effects at the endothelial tissue level.

Results and discussion

Formation of endothelial cell pairs

Cell pairs, or two cells with a shared junction, serve as the basic functional repeating unit of a continuous tissue such as the vascular endothelium (Fig. 1a). Here, endothelial cell pairs with defined morphologies were produced by seeding human umbilical vein endothelial cells (HUVECs) on protein micropattern arrays on a 2D substrate. Fibronectin (FN) is among the ECM components that facilitates the attachment of vascular endothelial cells to the basement membrane and supports tension-mediated processes that lead to changes in cell shape and proliferation.[28,29] FN islands were shaped as two adjacent hexagons with a single shared edge (Fig. 1a–c); the hexagonal shape mimics the polygonal, cobblestone-like shape of confluent endothelial cells which maximizes the number of adjacent cells under physiological conditions.[30] The microcontact-printed FN islands on polydimethylsiloxane (PDMS)-coated glass substrates were then seeded with HUVECs to form cell pairs confined in bihexagonal patterns. The cell pairs that underwent structural analysis were screened based on the following criteria: (i) the FN island underlying the pair had a bihexagonal shape without defects; (ii) the island contained two cells as evidenced by the presence of two nuclei, where each cell was confined to a single hexagon of the island; and (iii) the two cells were directly adjacent to one another, with their cell–cell junction area being within 45° to 90° of the long axis of the cell pair. Selecting for this specific orientation enables a systematic comparison of shape- and orientation-dependent structural parameters that can be measured from the images of immunostained cell pairs under different exposure conditions. Additionally, imposing these criteria normalizes intercellular tension between selected cell pairs, as junction length and strength may vary with junction orientation and are affected by cellular tension.[31,32] However, it is worth noting that the pair model does not account for the effect of multiple adjacent cells bordering one cell in the native endothelium; this is instead simplified as a one-neighbor/one-shared barrier model to increase the throughput of the assay model.

To promote the formation of cell pairs in this arrangement, each hexagon of the FN island had an area of 2500 μm^2, in accordance with the island area used to isolate single endothelial cells in previous studies.[33,34] In addition to the shape

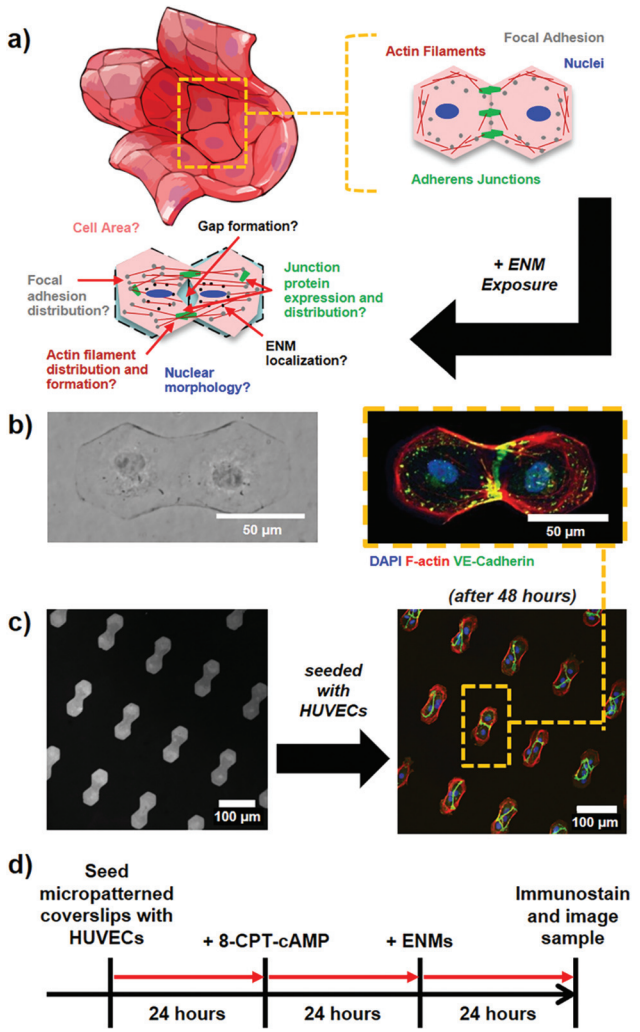

Fig. 1 Formation of endothelial cell pairs on micropatterned substrates. (a) Schematic illustration of cell pairs as a functional repeating unit of the vascular endothelium and the local structural parameters that can be assessed following ENM exposure. (b) Representative phase contrast and confocal images of an endothelial cell pair. Healthy endothelial cell pairs formed adherens junctions at the cell–cell contact border and expressed filamentous actin (F-actin) around the cell cortex. (c) PDMS substrate patterned with double hexagon FN islands (area = 2500 μm^2 per hexagon) prior to endothelial cell seeding and 48 hours after seeding. (d) Experimental timeline for endothelial cell pair ENM exposure studies.

being biomimetic, a hexagonal morphology was selected to impose a low aspect ratio to the cells, which minimizes any increase in cell stiffness that can occur prior to ENM exposure when endothelial cells are forced to conform to shapes with higher aspect ratios.[35] All experiments were conducted in static culture conditions, such that any observed changes following ENM exposure would be independent of the influence of shear stress on endothelial cell morphology. Following a 72 h culture period without ENM exposure (Fig. 1d), an average of 13.96 ± 0.84% of the FN islands on a coverslip contained cell pairs confined in the specified orientation eligible for screening using our assay (n = 55 images, 5 fields of view from 11 substrates).

Intracellular localization and cytotoxic effects of ENMs

After a 48 h culture period, the cell pairs were exposed to ENM dispersions for an additional 24 hours (except for the control, unexposed cell pairs). To demonstrate the broad utility of this assay for screening multiple nanomaterials, HUVEC pairs were exposed to 10 different ENMs of varying sizes and composition. This library of ENMs includes metals (Au, 18 nm; citrate-capped Ag, 22 nm) and metal oxides (TiO_2, 29 nm; ZnO, 46 nm; SiO_2, 15 nm; CuO, 50 nm; Fe_2O_3, 10 nm; Al_2O_3, 28 nm), as well as polymorphs of an organic nanomaterial—nanocellulose (cellulose nanocrystals, CNC, 250 nm × 25 nm; cellulose nanofibrils, CNF, 50 nm). These ENMs are commonly used for commercial applications, and therefore are good representative samples for developing a generalizable ENM toxicity screening platform.

To assess the dose-dependency of the ENM-induced effects on endothelial cell architecture, three ENMs were selected from this library to represent different ENM types: citrate-capped Ag nanoparticles (NPs), photocatalytic-grade TiO_2 NPs, and CNC as representatives of metal, metal oxide and organic nanomaterials, respectively. In our previous work, Ag and TiO_2 at 100 μg mL^{-1} were shown to have significant effects on the contractility of cardiac tissues, providing further reasoning for screening these ENMs for their effects on vascular barrier cells.[36] Currently, nanomaterial-induced damage has been attributed to either (1) oxidative stress due to reactive oxygen species (ROS) formation, or (2) disruption of cell–cell junctions, in conjunction with actin cytoskeleton remodeling.[11,37–39] Surface chemistry and size have a significant influence on the mechanism of action of permeability-inducing ENMs.[40] Metal oxides such as ZnO, CuO and Fe_2O_3 were previously reported to induce increases in intracellular ROS levels resulting in endothelial barrier gap formation.[7,37] On the other hand, TiO_2 and SiO_2 have been reported to physically interact with cell–cell junctions, resulting in intercellular gaps or inducing a signaling cascade that increases endothelial permeability.[11,38,41] Interactions of nanocellulose with endothelial cells are less studied than the other inorganic nanoparticles reported here, but previous reports suggest that they do not have significant cytotoxic effects on endothelial cells.[42] Regardless of the mechanism, alterations in cellular structure precede the disruption of endothelial barrier function. In the subsequent sections, such cellular-level changes induced by the aforementioned test ENMs will be quantified using micropatterned cell pairs.

Using darkfield imaging, representative ENMs internalized by cells and displaying significant optical scattering (TiO_2, Fe_2O_3, SiO_2) were observed to have a high propensity for localization in the perinuclear region (Fig. 2a), which is consistent with previous reports.[43–46] Due to the size range of the metal and metal oxide particles studied (~15 nm to 50 nm), the observed perinuclear localization is further rationalized by the inability of ENMs to translocate across the nuclear membrane, which hasf pore sizes (~5.2 nm) that may not be large enough for the ENMs studied herein.[47] The cytotoxic effects of the

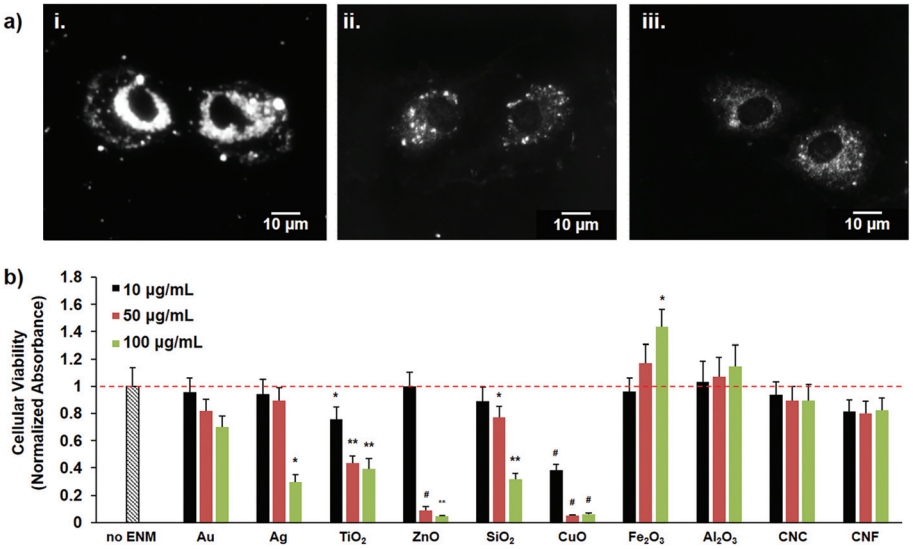

Fig. 2 Distribution of ENMs in cell pairs following exposure and their cytotoxic effects. (a) Representative darkfield images of cell pairs exposed to 10 μg mL^{-1} of (i) TiO_2, (ii) Fe_2O_3 and (iii) SiO_2. (b) Cellular viability of unpatterned HUVECs after exposure to ENMs for 24 h, as determined by MTS assay; absorbance measurements normalized against the unexposed (no ENM) condition. Error bars represent standard error of mean; $n \geq 3$ per exposure condition, where n is the number of wells per exposure condition. Red dashed line represents the value for no ENM condition. For statistical comparison, $*p < 0.05$, $**p < 0.005$, $\#p < 0.001$ with respect to control.

selected ENMs were then measured at different exposure levels (10 to 100 μg mL^{-1}) within a 24 h duration, in order to observe any dose-dependent trends for each ENM type. First, a colorimetric assay based on 3-(4,5-dimethylthiazol-2-yl)-5-(3-carboxymethoxyphenyl)-2-(4-sulfophenyl)-2*H*-tetrazolium (MTS) was used on unpatterned HUVECs to assess dose-dependent ENM cytotoxicity. The measured absorption of MTS-treated culture media correlates to mitochondrial reductase activity, and therefore to cellular viability. For most metal/metal oxide particles studied here, a dose-dependent decrease in cellular viability was observed, the two exceptions being Fe_2O_3 and Al_2O_3 (Fig. 2b). Though only Fe_2O_3 exposure at 100 μg mL^{-1} caused a statistically significant increase in absorption, the general increase observed post-Fe_2O_3 and Al_2O_3 exposure suggests an increase in metabolic stress similar to what has been previously reported for other nanomaterials.[48] The increase in metabolic stress as Fe_2O_3 dose increases is also consistent with a previous report which showed that Fe_2O_3 nanoparticles enhance endothelial permeability by promoting ROS-induced microtubule remodeling.[7] No significant decrease in cellular viability was detected for either nanocellulose polymorph.

In addition, all of the ENMs induced a significant increase in release of lactate dehydrogenase (LDH, a necrotic marker) with respect to the unexposed case, except for Ag at 10 μg mL^{-1} (ESI Fig. S1a and b†). Most notable LDH increases were observed for Ag (100 μg mL^{-1}), TiO_2 (50 and 100 μg mL^{-1}), ZnO (10 μg mL^{-1}) and CuO (10 μg mL^{-1})—all of which are consistent with the decreased mitochondrial reductase activity detected using the MTS assay. Increasing LDH release trends were also measured for Fe_2O_3 and Al_2O_3, which are the ENMs that showed increasing metabolic activity with increasing ENM dosage. These data suggest that HUVECs exposed to Fe_2O_3 or Al_2O_3 undergo increases in metabolic stress and cell death at higher ENM dosages. In addition, the expression of Ki67 in HUVECs with and without ENM exposure was measured to compare cellular proliferation across the exposure conditions (ESI Fig. S1c and d†) and to demonstrate that the two cell-limit per island is maintained throughout the 72 h experiment as per our analysis population criteria (see Fig. 1d for experimental timeline). An increase in cell proliferation could increase the number of FN islands per field of view that contain more than two cells, which do not meet our criteria for analysis. Among the library of ENMs tested, no significant increase in Ki67 expression was measured except under TiO_2 (100 μg mL^{-1}), CuO (10 μg mL^{-1}), and Al_2O_3 (10 μg mL^{-1}) exposure as compared to the unexposed control. These ENMs also caused an increase in LDH release, which may imply the necrotic cells under these exposure conditions have less contact inhibition, resulting in increased propensity to proliferate. On the other hand, less Ki67-positive cells were observed at higher doses of Fe_2O_3 (50 and 100 μg mL^{-1}). These data suggest that the majority of ENMs studied here do not significantly increase the propensity of HUVECs to proliferate over the course of the 24-hour ENM exposure period, therefore validating that the cell count per FN island is maintained throughout the assay.

ENM-induced changes in cellular morphology

Because cellular retraction correlates to increased barrier permeability and increased isometric tension exerted by cytoskeletal actin networks, ENM-induced changes in HUVEC pair cell morphology were measured under different exposure conditions.[49] Here, morphological changes in the cell pairs were quantified from the ratio between the total area of each cell

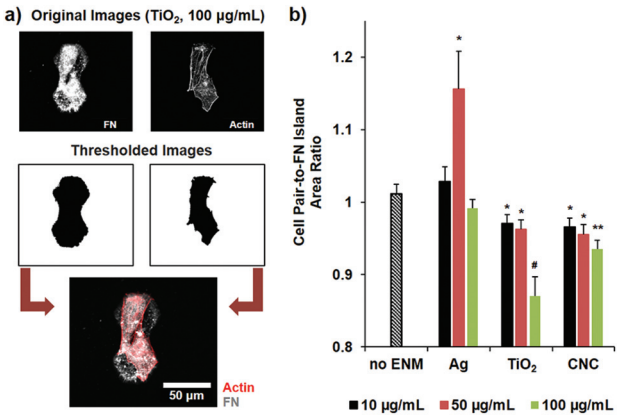

Fig. 3 Impact of ENM exposure on the response of endothelial cells to extracellular shape cue. (a) Schematic diagram of analysis method for calculating the cell pair-to-FN area ratio (AR). After thresholding FN and F-actin cell pair images, the cell pair area and fibronectin island area were measured, and the ratio was calculated. (b) AR values following exposure to Ag, TiO_2, and CNC at 10, 50, and 100 μg mL^{-1} ($n \geq 30$, where n is the number of cell pairs per exposure condition). For statistical comparison, $*p < 0.05$, $**p < 0.005$, $\#p < 0.001$ with respect to control.

pair and the underlying FN island. This evaluation is important for determining the direct effect of ENMs on morphology and in assessing the integrity of adhesion of endothelial cells to basement membrane ECM proteins.[50] The cell pair-to-FN island area ratio (AR) was measured through analyzing actin- and FN-stained cell pair images (Fig. 3a). The dose-dependent effects of Ag, TiO_2 and CNC on cellular morphology were also quantified using our cell pair model (ESI Fig. S2† and Fig. 3b). Among the library of ENMs tested, Au, TiO_2, ZnO and Al_2O_3 induced a significant decrease in AR at 10 μg mL^{-1} (ESI Fig. S3†), while Ag caused an increase in this ratio. While a decrease in AR value may be attributed to the onset of decreased cellular viability, either cellular retraction or expansion can occur due to cytoskeletal rearrangement when ENMs accumulate within the perinuclear region of the cell. Due to the dynamic nature of cell spreading or retraction, we account for temporal variability in cell morphology by averaging at least 20 cell pairs from two separate biological replicates per analysis.

In the case of TiO_2 and CNC, a decrease in AR was observed with increasing ENM dosage (Fig. 3b). While the cell retraction with increasing TiO_2 dosage corresponds to the observed decrease in cell viability (Fig. 2b), the change in AR values when exposed to CNCs cannot be attributed to a decrease in cell viability. This observation is similar to the case of Au, TiO_2, ZnO and Al_2O_3 at 10 μg mL^{-1}. ENM screening using the micropatterned pair model therefore allows the detection of significant structural changes even at doses that do not affect cellular viability, such as in the case of CNC exposure. Interestingly, exposure to Ag NPs at 50 μg mL^{-1} induced a dramatic increase in AR value corresponding to cellular expansion, but decreases again at 100 μg mL^{-1} when a significant number of cells begin to undergo cell death. Therefore, these observed cellular behaviors caused by ENM exposure cannot solely be attributed to effects on cellular viability, but may also be due to the activation of GTPase-dependent pathways that lead to cytoskeletal reorganization.[51] Due to these findings, in which the cells failed to abide by the ECM protein adhesion and shape cues, ENM-induced endothelial cytoskeletal remodeling was further investigated as a potential explanation for this behavior.

Remodeling of cytoskeletal organization due to ENM exposure

To study cytoskeletal remodeling due to ENM exposure, changes in the organization and intracellular distribution of actin filaments were quantified. Actomyosin contraction regulates the permeability of endothelial layers. Filamentous actin at the periphery of cells (cortical actin) serves as an important supporting network in intercellular junction formation and cell–ECM adhesion,[52] while contractile stress fibers are distributed across the cell body and develop in response to permeability-increasing agents.[49,53,54] Particularly, it is well-supported that stress fiber formation is induced during myosin light-chain kinase and RhoA-Rho kinase pathway activation, which consequently disrupts the integrity of adherens junctions.[49] Considering that the cytoskeleton has a vital role in shaping cellular architecture and in maintaining the barrier integrity of endothelial tissues, quantifying changes in actin organization and stress fiber formation is an important probe for screening ENMs that can compromise the barrier function of endothelial cells. Previously, it has been reported that certain nanoparticles can lead to actin fiber reorganization, resulting in increased endothelial layer permeability.[9] Here, we hypothesize that ENM exposure may disrupt barrier function by shifting the distribution of polymerized actin in endothelial cells from cortical rings to central stress fibers.

Cell pair actin distribution maps were generated by compiling actin-stained images for each exposure condition into average intensity composites (Fig. 4 and ESI Fig. S4, S5†). The radial actin distribution from the center of each FN hexagon composing the cell pair island (Fig. 4g and ESI Fig. S6–S10†) was then quantified for each ENM type. Two additional control groups were used as a point of comparison: cell pairs treated with (i) calpeptin, a Rho activating drug, which increases stress fiber formation; and (ii) Y-27632, a ROCK inhibiting drug, which disrupts cortical actin formation (ESI Fig. S7†). Results show a significant increase in fluorescence signal from actin staining in the central region (0 to 15.5 μm from the center of each hexagon) and a decrease in the peripheral region (15.5 to 31 μm), following exposure to most ENMs at 10 μg mL^{-1}, except for Au (Fig. 4g and ESI Fig. S9 and S10†). Additionally, a dose-dependent increase in stress fiber formation was observed as the ENM dose increased for Ag, TiO_2 and CNC (Fig. 4d–f). At the cell–cell junctions, actin intensity was also significantly greater after exposure to different doses of Ag, TiO_2 and CNC (ESI Fig. S11†). In the case of Ag at 100 μg mL^{-1}, where the cell viability is considerably low, the highly localized central signal that is non-filamentous in nature can be attributed to the depolymerization of actin during cellular death. Nonetheless, in most cases, increasing the ENM con-

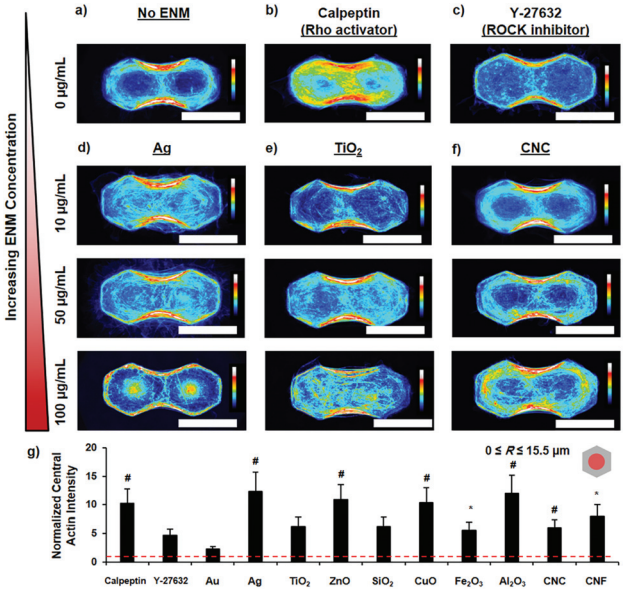

Fig. 4 Dose-dependent effect of ENM exposure on actin filament distribution in endothelial cell pairs. Composite confocal images of cell pairs immunostained against F-actin; (a) without ENM exposure, (b) with calpeptin (a Rho activating drug, induces stress fiber formation), (c) with Y-27632 (a ROCK inhibiting drug, disrupts cortical actin), and those exposed to 10 μg mL^{-1}, 50 μg mL^{-1}, and 100 μg mL^{-1} (d) Ag, (e) TiO_2 and (f) CNC for 24 hours. Scale bars = 50 μm; $n \geq 20$ per composite heat map, where n is the number of cell pairs per exposure condition. (g) Quantification of actin distribution in the central region (inset: red highlighted area, radius, R = 0 to 15.5 μm from the center of a hexagonal cell) of ENM-exposed (10 μg mL^{-1}) patterned cells using radial scanning; normalized against the values for unexposed cell pairs (red dashed line). For statistical comparison, $*p < 0.05$, $**p < 0.005$, $\#p < 0.001$ with respect to control.

centration leads to an observable transition from predominantly cortical actin to the formation stress fibers reminiscent of faulty endothelial barriers.

The expression of vinculin, an important protein in focal adhesion complexes, was also assessed in the ENM-exposed and unexposed HUVEC pairs (ESI Fig. S12†). Mapping the distribution of focal adhesion proteins such as vinculin offers insight into the impact of ENMs on cellular tension, because focal adhesion complexes are force-generating and tension-bearing structures.[55] Immunostained vinculin features that are filamentous or elongated in nature were predominantly colocalized with actin fibers (ESI Fig. S12 and S13†). As expected, calpeptin-exposed (Rho-activated) and Y-27632-exposed (ROCK-inhibited) pairs showed increased and decreased formation respectively of these features in the cell periphery relative to unexposed pairs (ESI Fig. S14†). However, these elongated vinculin features indicative of focal adhesions were less pronounced at the cell edges for Ag-exposed HUVEC pairs as compared to unexposed pairs. In addition, decreased vinculin localization at the junction area is particularly notable in cell pairs exposed to all doses of Ag.

To gain a more specific and quantitative understanding of vinculin expression in the cell pairs (pre- and post-ENM exposure), we measured vinculin distribution within the pairs using a modified version of the method used to analyze actin distribution. Because of non-specific vinculin staining observed largely in the middle of the cells, we conducted this analysis on the periphery of the outer half of each pair (ESI Fig. S15†). The cell periphery for the distribution analysis here covers R = 15.5 μm to 26.9 μm (an inscribed circle), as opposed to 31 μm to reduce the number of potentially null pixels profiled. In agreement with the observations made based on the vinculin heat maps, calpeptin-exposed pairs showed increased peripheral vinculin, while Ag and TiO_2-exposed pairs showed decreased peripheral vinculin at all exposure levels. Because actin-bound vinculin is associated with both cell–cell and cell–ECM adhesions,[56] the reduction of peripheral vinculin expression could be a cellular response to maintain balance in intracellular and paracellular tension during ENM exposure, which is consistent with previous reports.[9,22,57]

Interestingly, immunostaining against FN showed features reminiscent of the distribution patterns observed in actin and vinculin across the cell pairs. These cellular artefacts, which were not observed on FN patterns without cells (Fig. 5a), provide evidence of cells adhering to the substrate at localized points (*i.e.*, *via* focal adhesion complexes). The appearance of these artefacts is consistent with the known ability of endothelial cell to rearrange exogenous fibronectin.[34] These features were then used as an indicator for the distribution of tension-bearing structures within cell. In particular, the colocalization of vinculin-FN pixels from the images of immunostained cell pairs was measured as a metric for cell–ECM adhesion and to validate the observed changes in vinculin localization after ENM exposure (Fig. 5b and c). Using vinculin-FN colocalization to quantify focal adhesion distribution also further mitigated the effects of non-specific vinculin staining, thus providing a more specific metric than vinculin pixel intensity alone.

To assess changes in distribution of tension-bearing features within cell pairs (*i.e.*, localized at the edge or at the center), radial distribution profiles were generated for all vinculin-FN colocalization images (ESI Fig. S16†). Consistent with the vinculin distribution results, peripheral vinculin-FN colocalized pixel intensity was significantly decreased in Ag- and TiO_2-exposed pairs at all doses relative to the unexposed controls. Contrary to the vinculin-only analysis, calpeptin induced a decrease in relative colocalized pixel intensity between exposed and unexposed pairs. This inconsistency suggests that the results of these two methods of analysis (distribution of vinculin-only *vs.* vinculin-FN colocalized pixels) may vary if pairs are exposed to factors that induce marked increase in focal adhesion density such as calpeptin. Though the differences between the pixel intensities in CNC-exposed and unexposed pairs were statistically significant, no clearly observable trend in variation was observed.

At the highest Ag concentration (100 μg mL^{-1}) and for calpeptin-exposed samples, total (non-region specific)% colocalization of vinculin and FN was significantly higher than in the unexposed condition (ESI Fig. S17†). The former may be

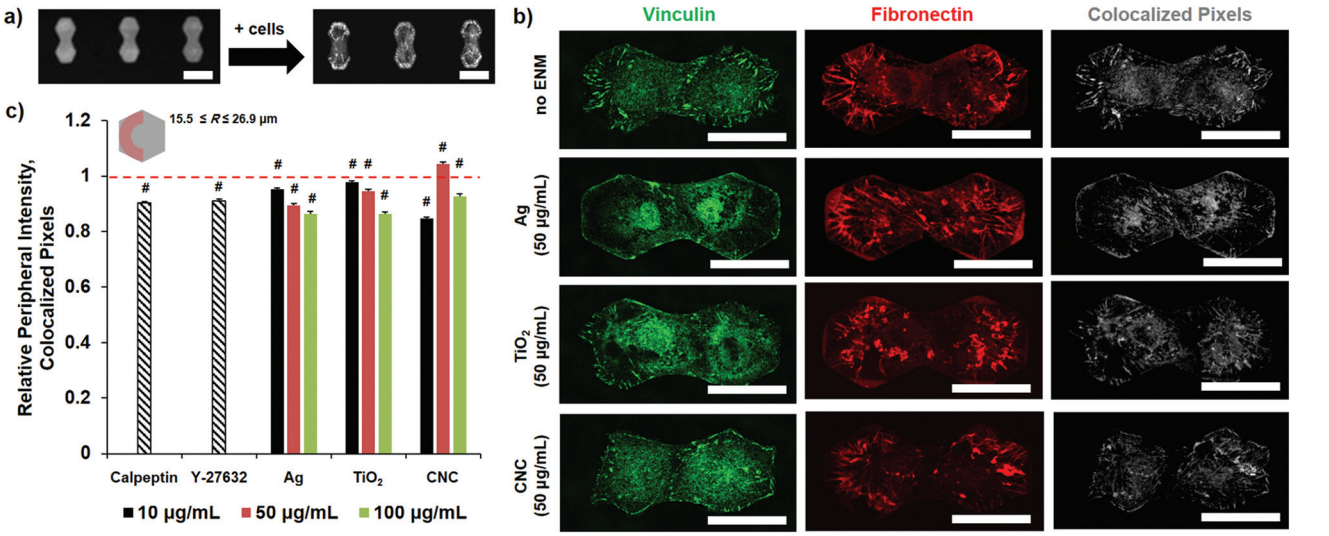

Fig. 5 Distribution of colocalized vinculin and fibronectin features. (a) Micropatterned bihexagonal FN island images (immunostained against FN) before and 72 h after cell seeding; scale bars = 100 μm. (b) Representative images of cell pairs exposed to Ag, TiO_2 and CNC at 0 and 50 μg mL^{-1}, immunostained against vinculin and FN; scale bars = 50 μm. Colocalization of vinculin and FN pixels were defined using Costes method (see ESI†). (c) Relative peripheral intensity of colocalized vinculin and FN pixels (with respect to total vinculin pixels) for cell pairs under different exposure conditions (inset: peripheral region pertains to the red highlighted area, R = 15.5 to 26.9 μm of one cell). Red dashed line represents the measurement of unexposed cell pairs (no ENM); $n \geq 10$, where n is the number of cell pairs per exposure condition.

attributable to cell protein rearrangement following cell death, similar to the actin rearrangement shown in Fig. 4d. The latter is likely the result of increased focal adhesion formation in the Rho-activated pairs. CNC exposure at 50 and 100 μg mL^{-1} was also associated with a significant increase in % colocalization, which is likely a byproduct of increased stress fiber formation (see ESI Fig. S9†) and thereby increased focal adhesion formation, as would be the expected response in an otherwise normal cell. No trend in vinculin-FN colocalization was observed with respect to TiO_2 dosage. Altogether, we show how this micropatterning-based assay enables the quantification of stress fiber formation and the distribution of vinculin expression—both of which are factors that suggest changes in the organization of tension-bearing cytoskeletal proteins in response to ENM exposure as an external stimulus.

Changes in nuclear morphology and separation post-ENM exposure

Remodeling of the cytoskeleton can influence nuclear morphology *via* direct linkages between the nuclear lamina and cytoskeleton, which could in turn modify chromatin dynamics, gene expression, as well as mechanical homeostasis.[58–61] Given that several of the ENMs tested here induced changes in endothelial actin distribution and stress fiber formation, we next sought to determine whether ENM exposure had any effect on nuclear morphology and internuclear separation. Because the actin networks of two cells are mechanically tethered to one another *via* actin-associated adherens junctions, and to their respective nuclear lamina *via* linker proteins bridging the nuclear envelope,[59,60] we hypothesized that ENM-induced actin remodeling could lead to changes in nuclear eccentricity. Previous work has demonstrated that nuclear elongation can occur as the result of combined lateral compressive and longitudinal elongation forces applied by stress fibers in endothelial cells.[62] We therefore used the cell pair model to systematically measure changes in nuclear eccentricity as a function of ENM dosage. Additionally, the assay was used to test whether exposure to select ENMs leads to changes in internuclear separation and nuclear morphology (Fig. 6a). We define internuclear separation as the distance between the center of the nuclei of the two cells in the pair (Fig. 6b). Nuclear eccentricity was measured by fitting nuclei to ellipses as previously described (Fig. 6c).[63]

After exposing the cell pairs to each of the 10 ENMs at a low concentration (10 μg mL^{-1}), only TiO_2 and SiO_2 NPs induced a significant increase in internuclear separation (ESI Fig. S18a†). A significant increase in internuclear separation was also observed after exposing the pairs to Ag NPs at a high concentration (100 μg mL^{-1}, Fig. 6d). Because contractile actomyosin fibers bind cell nuclei and adherens junctions *via* interactions with VE-cadherin/catenin protein complexes,[64,65] it is possible that the contraction of these fibers following Ag NP exposure at 10 and 50 μg mL^{-1} decreases internuclear separation, while non-filamentous actin aggregates observed after exposure at 100 μg mL^{-1} (Fig. 4d) do not create this effect. While CNC exposure did not result in any significant changes in nuclear parameters, TiO_2 exposure resulted in a dose-dependent decrease in internuclear separation distance following an initial increase at the 10 μg mL^{-1} dosage (Fig. 6d). Given that more stress fibers formed with increasing TiO_2 exposure (Fig. 4e), contraction of these fibers could draw the nuclei together and result in this downward trend.

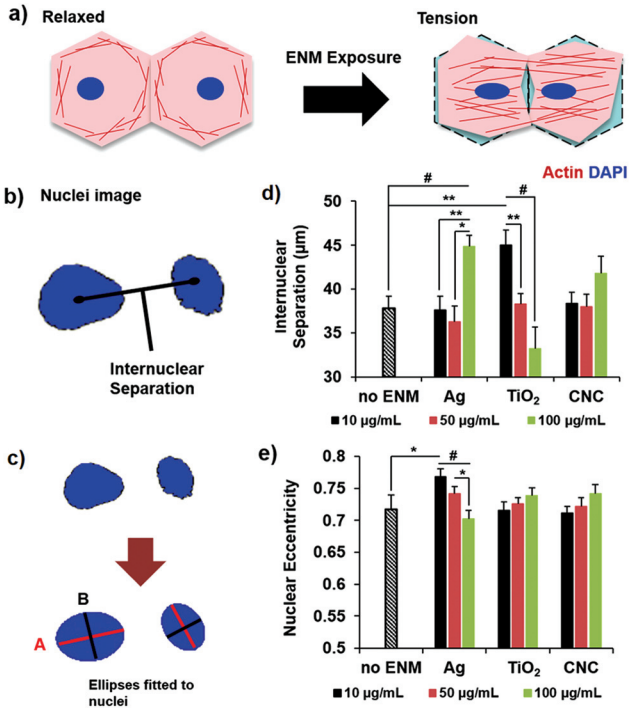

Fig. 6 Dose-dependent effect of ENM exposure on distance between endothelial cell pair nuclei and nuclear eccentricity. (a) Illustration of tension-induced nuclear remodeling of cell pairs following ENM exposure. (b) Schematic diagram depicting the analysis procedure used to determine cell pair internuclear separation. Internuclear separation was defined as the distance between the centers of the nuclei of the two cells. (c) Schematic diagram depicting nuclei fitted to ellipses for measuring nuclear eccentricity, resulting in values from 0 to 1, where 0 corresponds to a circle. (d) Internuclear separation following exposure to Ag, TiO_2, and CNC at 10, 50, and 100 μg mL^{-1} ($n \geq 20$, where n is the number of cell pairs per exposure condition). (e) Nuclear eccentricity following exposure to Ag, TiO_2, and CNC at 10, 50, and 100 μg mL^{-1} ($n \geq 40$, where n is the total number of cells per exposure condition). For statistical comparison, $*p < 0.05$, $**p < 0.005$, $\#p < 0.001$.

While most ENMs did not show any statistically significant changes in nuclear eccentricity in comparison to unexposed samples, increased nuclear elongation was observed after Ag NP exposure at 10 μg mL^{-1} (Fig. 6e and ESI Fig. S18b†). Contrary to what was expected due to increased stress fiber formation, eccentricity of the cell pair nuclei trended downwards with increasing Ag NP dosage following this initial increase. This effect may be because increasing the dosage of Ag increased the rate of cell death, as well as the degradation rate of the actin cytoskeleton which occurs during the final stages of this process.[66,67] This observation is consistent with higher cytotoxicity and apoptotic activity following Ag exposure relative to TiO_2 and CNC (Fig. 2b and ESI Fig. S1a†), as well as the appearance of the previously mentioned non-filamentous actin aggregates in the cell pairs exposed to Ag NPs at 50 and 100 μg mL^{-1}. Although TiO_2 and CNCs induced nominal increases in nuclear eccentricity as the dosage level increased from 10 to 100 μg mL^{-1}, the trends were not statistically significant. Together, these results show that our micropatterned model offers a way to not only measure changes in nuclear eccentricity, but also to systematically quantify the internuclear separation between paired cells.

ENM effects on the formation of adherens junctions and intercellular gaps

Lastly, the direct impact of ENMs on the formation of endothelial adherens junctions, which have an important role in the control of paracellular transport, was investigated using the cell pair model. Actin filaments are tightly linked to these junctions; therefore, an orchestrated balance in tension within this network is required for proper tissue development and homeostasis.[68] When quantifying ENM-induced changes in cell–cell junction features, our HUVEC pair model presents the advantage of having cells constrained to a defined area and orientation, resulting in cell–cell contacts being in approximately the same location and of the same length in each pair. Considering that the formation of adherens junctions is the result of calcium-dependent homophilic interactions between vascular endothelial (VE)-cadherins in adjacent cells,[69,70] the fluorescence intensity of immunostained VE-cadherins was systematically measured along the intercellular junction area of the cell pairs. To observe VE-cadherin expression, the cell pairs were stained with an anti-VE-cadherin antibody which binds VE-cadherin independent of its dimerization state. VE-cadherin junction area expression was quantified by first creating a linear profile along the midline of the junction area for an analyzed pair, and then calculating the mean intensity of the pixels along the length of this profile (Fig. 7a). The reported values were averaged from these measured mean intensities, then normalized with respect to the unexposed cell pairs. Confocal imaging conditions were made consistent across all samples.

A significant decrease in intercellular junctional VE-cadherin expression intensity was observed following exposure to CNC at 10 μg mL^{-1} (0.92 ± 0.02 *vs.* 1 ± 0.02 in unexposed samples), but no significant decrease was measured for any of the other ENMs tested at this dosage level (Fig. 7b and ESI Fig. S19a†).[71] When cell pairs were exposed to higher dosages of Ag, TiO_2, and CNC, a decreasing VE-cadherin junction expression intensity was measured as the dose increased from at 10 to 100 μg mL^{-1} (Fig. 7b). These results suggest that each of these three nanomaterials have a negative and dose-dependent impact on the formation of endothelial adherens junctions.

Given that a decrease in adherens junction formation diminishes the strength of cell–cell interactions, we next asked whether ENM exposure results in any structural changes at the cell–cell junctions, such as the formation of intercellular endothelial gaps. Formation of endothelial gaps *in vivo* provide a pathway for protein, fluid, and inflammatory cell leakage into body tissues, resulting in a pathophysiological imbalance in both fluid homeostasis and inflammatory cell activity. Intercellular gap formation was measured by identifying regions of interest within actin-stained images of cell pairs where separation between the edges of the two cells was visible despite the possibility of cell–cell contact, thresholding

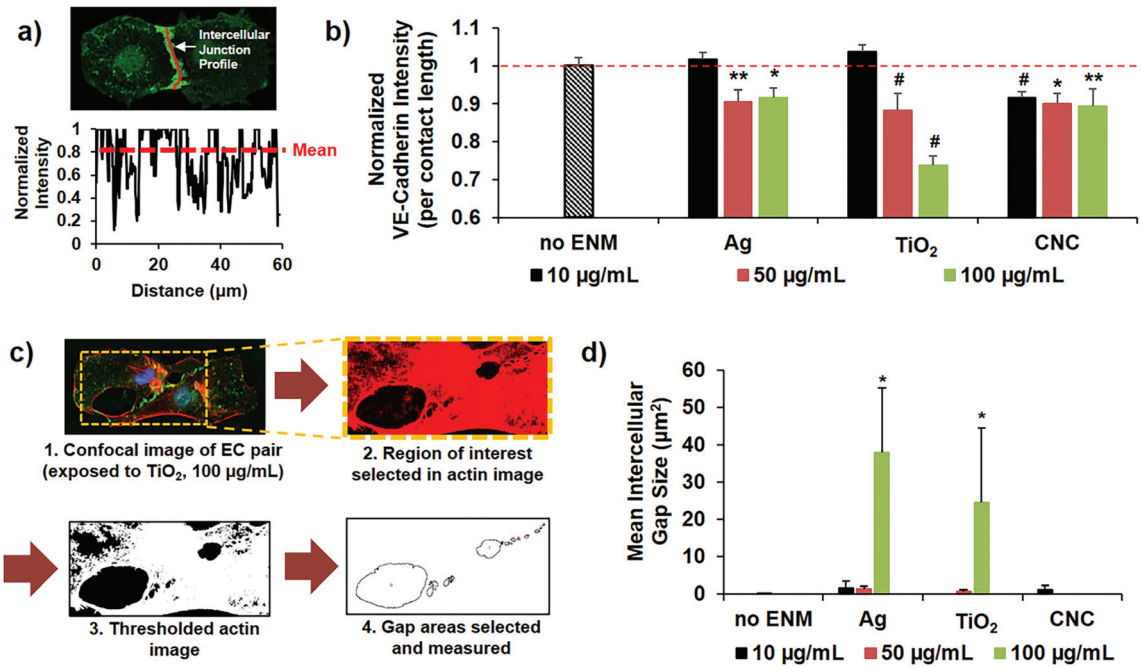

Fig. 7 Changes in VE-cadherin expression and formation of intercellular gaps between endothelial cell pairs due to ENM exposure. (a) Procedure for measuring VE-cadherin expression intensity per contact length in the intercellular junction area. A linear profile was created along the midline of the junction area for each analyzed pair and the mean intensity of the pixels along the profile was calculated. The values reported are an average of these measured mean intensities, normalized with respect to the unexposed cell pairs. (b) VE-cadherin intensity per contact length following exposure to Ag, TiO_2, and CNC at 10, 50, and 100 μg mL^{-1} ($n \geq 20$, where n is the number of cell pairs per exposure condition). Red dashed line represents the value for no ENM condition. (c) Procedure for measuring intercellular gap size in EC pairs. (d) Mean intercellular gap size following exposure to Ag, TiO_2, and CNC at 10, 50, and 100 μg mL^{-1} ($n \geq 20$, where n is the number of cell pairs per exposure condition. For statistical comparison, *$p < 0.05$, **$p < 0.005$, #$p < 0.001$ with respect to control.

the image, and measuring the total area of the observed gaps (Fig. 7c). Mean intercellular gap area is defined as the total gap area observed in all pairs analyzed divided by the number of pairs analyzed, as opposed to the number of gaps observed. This accounts for the variation in frequency of gap occurrence per pair. The sample size is reported as the number of pairs containing at least one gap with a minimum area of 2 μm^2, which was the average area of small gaps in the intercellular junctional area that were visible in VE-cadherin-stained cell pair images regardless of ENM exposure. No significant gap formation was observed following exposure to any of the ENMs at 10 μg mL^{-1} (ESI Fig. S19b†). This result is consistent with the absence of changes in intercellular junctional VE-cadherin expression intensity following exposure to all ENMs tested at this dosage level, with the exception of CNC. Significant intercellular gap formation was observed following exposure to Ag and TiO_2 NP at 100 μg mL^{-1}, with the mean gap size induced by Ag NPs (37.93 ± 17.18 μm^2) being nominally larger than that induced by TiO_2 NPs (24.42 ± 20.04 μm^2) (Fig. 7d and ESI Fig. S20 and S21†).

The findings discussed above were consistent with a previous report, demonstrating that TiO_2 reduces junctional VE-cadherin expression leading to intercellular gap formation and increased endothelial permeability.[11] It was shown that TiO_2 NPs (23.5 μm diameter) directly bind to VE-cadherin in adherens junction, disrupting the VE-cadherin homodimer, which induces the phosphorylation of VE-cadherin at two protein residues and leads to internalization and degradation. Importantly, the gap formation and increased permeability were shown to be size-dependent, as TiO_2 microparticles (680 nm diameter) did not induce these effects, while both Ag NPs (20 nm diameter) and SiO_2 NPs (15 nm diameter) did. Given that the Ag and TiO_2 NPs tested here were similar in size (with diameters of 22 and 29 nm, respectively), it is possible that both NPs exert their effects through this mechanism, as supported by the previously-mentioned work[11] and other studies showing Ag-induced VE-cadherin internalization.[72,73] Other permeability-increasing and inflammatory agents have also been shown to induce VE-cadherin phosphorylation, internalization, and intercellular gap formation in endothelial cells.[74,75] However, in addition to differences in surface chemistry, the CNCs tested (250 nm) here are larger than the Ag and TiO_2 NPs, making it unlikely that the reduction in junctional VE-cadherin expression observed following CNC exposure is the result of the same direct binding mechanism. Previous studies have shown that CNCs exerted no cytotoxic effects on endothelial cells (consistent with our MTS assay results in Fig. 2b) and were not taken up by the cells.[76] In this case, it is possible that some other form of interaction between the nanocrystals and the extracellular domain of the VE-cadherin

proteins results in the significant decrease of VE-cadherin in the intercellular junctional area.

Many of the ENM-exposed pairs also showed the appearance of "discontinuous" adherens junctions (ESI Fig. S22†), or areas along the intercellular junction line where junctional proteins like VE-cadherin are distributed in short, linear structures that are approximately perpendicular to the cell border.[65] As opposed to being associated with cortical F-actin, such junctions are localized at the ends of stress fibers. Discontinuous adherens junction are formed by the structural transformation of existing adherens junctions *via* cortical actin remodeling.[64] Subsequently, the contraction of actomyosin fibers associated with discontinuous adherens junctions has been shown to induce junction deformation and the generation of intercellular gaps in endothelial tissues.[65,77] Multiple ENMs were shown to induce stress fiber formation in the EC pairs. Other than stimulating VE-cadherin homodimer dissociation *via* direct binding (as with Ag or TiO_2 NPs), ENM-induced stress fiber formation resulting in increased junctional tension and deformation is another potential mechanism by which ENM exposure contributes to both decreased VE-cadherin junction area expression intensity and intercellular gap formation as shown here.

Correlating assay parameters to tissue-level permeability

To compare ENM-induced cell- and tissue-level effects, the previously measured effects of ENMs on cellular structural features (Fig. 8, black traces) were correlated to their impact on

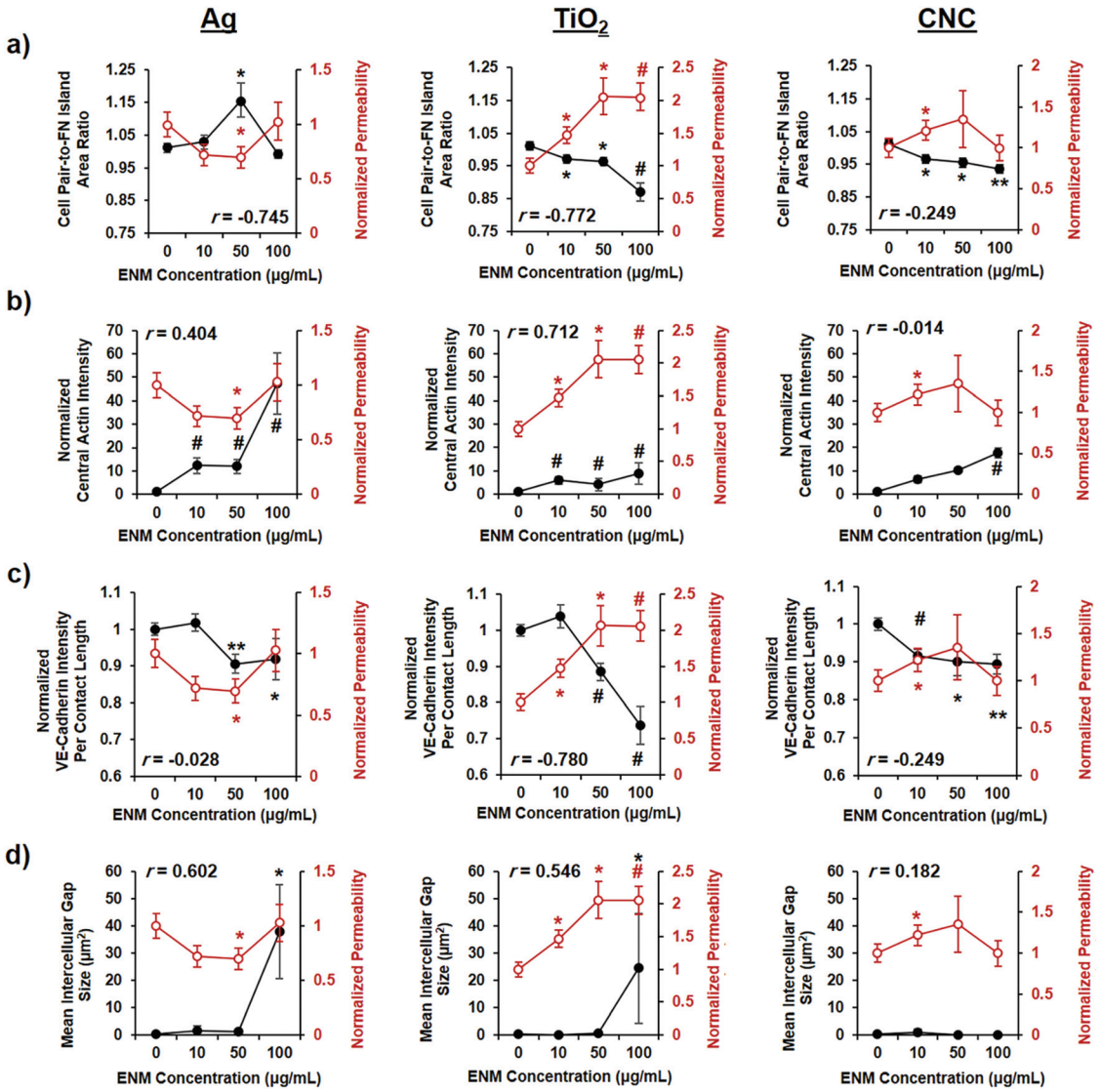

Fig. 8 Correlation plots: changes in cellular architecture correlated to endothelial barrier permeability. (a) Cell pair-to-FN island area ratio or AR, (b) central actin intensity ratio, (c) VE-cadherin expression intensity in intercellular junction area, and (d) mean intercellular gap size (all black) plotted with EC monolayer permeability (red, normalized with respect to unexposed conditions) as a function of ENM exposure level. For statistical comparison, *$p < 0.05$, **$p < 0.005$, #$p < 0.001$ with respect to control. The correlation coefficient, r, between the cellular architecture parameters and tissue permeability is reported in each plot.

HUVEC monolayer permeability (Fig. 8, red traces). The ENM-induced changes measured using the cell pair model and the endothelial monolayer permeability assay were also compared to assess the similarity in the gathered data trends from each approach. Tissue-level permeability measurements were acquired for HUVEC monolayers exposed under the same ENM dose range as in the cell pair studies (ESI Fig. S23†). For these measurements, HUVECs were grown on a Transwell membrane insert until confluency, after which the apical layers of these wells were subjected to Ag, TiO_2 and CNC exposure at 10, 50 and 100 μg mL^{-1} for 24 hours.

As expected, increasing endothelial monolayer permeability corresponded to decreasing AR or progressing cellular retraction as the TiO_2 dose increased (Fig. 8a). The TiO_2 dose-dependent increase in monolayer permeability also correlated to the increase in stress fiber formation, as measured from the centralized actin expression (Fig. 8b). These observations were consistent with the trends from the cytotoxicity data in Fig. 2, as well as with literature precedents that report a correlation between increased cellular tension due to the formation and contraction of stress fibers, to cell retraction and increased monolayer permeability.[52] The trends in the two junctional parameters quantified (decrease in VE-cadherin junctional area expression and increase in intercellular gap formation) also corresponded to increased monolayer permeability as the TiO_2 dosage was increased (Fig. 8c and d); with the most significant changes occurring between TiO_2 dosages of 50 and 100 μg mL^{-1} in both parameters. The TiO_2-exposed cell pairs also showed the highest correlation coefficients between the measured parameters and tissue permeability. However, no clear dose-dependent trends were observed in monolayer permeability following Ag NPs and CNC exposure despite the dose-dependent decrease in cellular viability due to Ag shown in Fig. 2. In the case of exposure with Ag NPs, the unusual decrease in permeability at 50 μg mL^{-1} can be explained by the measured increase in AR (Fig. 8a) and expansion of actin network (Fig. 8b). The permeability increases again when the cell viability significantly decreases at 100 μg mL^{-1} Ag exposure. Additionally, these data show that CNC exposure at 10 to 100 μg mL^{-1} leads to dose-dependent changes in cellular morphology, stress fiber formation, and VE-cadherin expression, but does not significantly affect cellular viability or tissue-level permeability (Fig. 8). Using the cell pair approach, we also assessed the structural impact of Fe_2O_3 (ESI Fig. S24†), which was previously reported to increase endothelial permeability by upregulating ROS production.[7] Our measurements show a strong inverse correlation ($r = -0.956$) between the dose-dependent changes in cell area and tissue permeability (ESI Fig. S24c†). These results are consistent with the cellular shrinkage caused by ROS formation, which eventually degrades endothelial barrier function. Taken together, these results across multiple types of ENMs demonstrate how this cell pair assay provides information on nanomaterial-induced changes in cellular architecture parameters that are not accessible using traditional cytotoxicity tests or assays based on monolayer tissues.

Finally, a similarity index scoring method was used to define a "healthy" cell pair phenotype based on the unexposed cells with completely formed adherens junctions. In particular, this method enables the quantification of the extent to which a cell pair deviates from the unexposed phenotype after ENM exposure for 24 hours. The index implements a modified implementation of the Hellinger distance formula, which is used to quantify the similarity between two probability distributions (see ESI† for the full discussion of the mathematical approach).[78] This index combines the metrics which we defined in the sections above to be important in screening whether an ENM induces dysfunction to an endothelial cell pair. The index score falls between 0 and 100, where a score of 0 indicates that the distributions are completely different (*i.e.*, no match between the exposed and unexposed cell pairs for that exposure condition), and a score of 100 indicates that the distributions are completely identical (*i.e.* a complete match between the exposed and unexposed cell pairs for that exposure condition). Despite the absence of dose-dependent trends for some individual parameters, the combined scores for each Ag and TiO_2 exposure condition showed a dose-dependent decrease that coincided with increasing monolayer permeability (Fig. 9). The observed collective trends for Ag and TiO_2 support how structural features of cells change in a con-

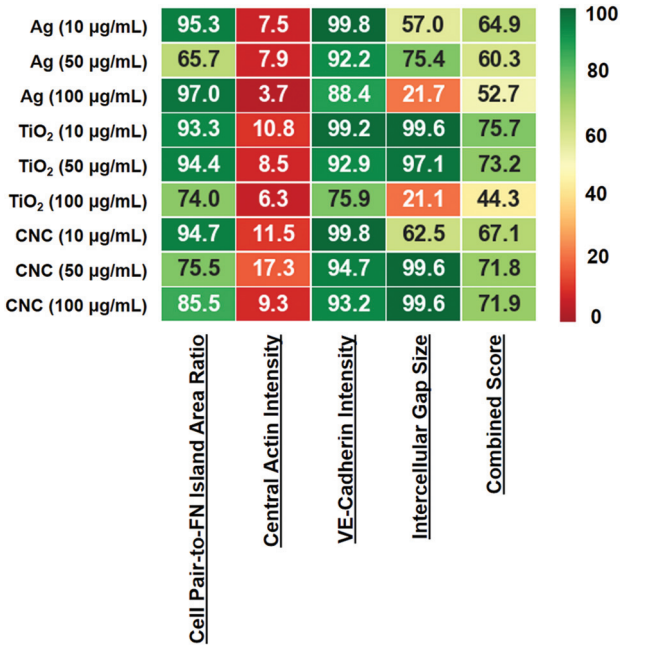

Fig. 9 Similarity index based on cell pair assay metrics. Cell pair scoring index, which compares the state of cell pairs exposed to different ENM conditions and those that are "healthy", unexposed endothelial cell pairs. The index is a modified implementation of the Hellinger distance formula, which is used to quantify the similarity between two probability distributions. A score of 100 indicates complete similarity between two data sets, while a score of 0 indicates complete dissimilarity. The combined score represents the average score from the following individual parameters: cell pair-to-FN island area ratio, central actin intensity, VE-cadherin intensity, and intercellular gap size.

certed manner and contribute to barrier dysfunction. Our model deconstructs the structural features of endothelial cell pairs into measurable parameters while the associated scoring method allows for quantitative comparisons between the effects of different ENM exposure conditions. Altogether, the scoring index implemented here enables quantitative comparisons of sample conditions imposed upon the cell pairs—allowing for the summative analysis of the effects of ENM exposure on endothelial cell morphology, ECM adhesion, actin distribution, and intercellular junction protein expression.

Conclusions

In this study, the influence of select ENMs on multiple key features of endothelial cell architecture and cell–cell junctions were quantified using a reductionist micropatterning assay. All measurements were performed on geometrically-controlled cell pairs with a specific orientation, which can be formed reproducibly by seeding HUVECs on bihexagonal micropatterns of a cell adhesion protein such as fibronectin. From these micropatterned endothelial cell pairs, changes in morphological features, nucleo-cytoskeletal organization and adherens junction formation after ENM exposure were measured. This approach revealed the connections between changes in multiple cellular features, as well as their correlation to changes in tissue-level endothelial barrier permeability upon exposure to ENMs at different doses. Using our assay, the extent to which the tested ENMs induce deviations from a healthy HUVEC pair phenotype were quantified using a "similarity index", which evaluates the overlap in values from two distributions of experimental data. Particularly, Ag and TiO_2 nanoparticles showed a dose-dependent decline in score, indicating increasing deviation from the unexposed phenotype. In the case of TiO_2, a dose-dependent trend was observed in cellular feature deviation, which also correlated with increasing tissue-level permeability. Overall, we have developed a quantitative assay based on micropatterned cell pairs, which aims to provide a clearer probe into changes in cellular-level features due to permeability-inducing agents such as some of the ENMs studied here. Importantly, this assay paves the way to consequently monitor changes in cell–cell interactions and cell–ECM adhesion during and after ENM exposure, which is rarely the case in traditional *in vitro* models of endothelial tissues. Therefore, this endothelial cell pair model and the associated assay can be useful towards standardizing the screening methods for assessing the effect of drugs and toxicants on cells with barrier-like function in physiological settings.

Experimental section

PDMS stamp fabrication

PDMS stamps for microcontact printing were prepared as previously described.[23] A photolithographic mask was designed in AutoCAD (Autodesk Inc.) and ordered from Output City (Brandon, OR, USA). Each mask consists of an array of bihexagonal islands with a single shared edge, each shape having a total area of 5000 μm^2 (hexagon edge length, 31 μm). This mask was imposed on top of a silicon wafer (Wafer World, FL, USA) spin-coated with SU-8 2002 negative photoresist (MicroChem Corp., MA, USA), which was then exposed to UV light to crosslink the pattern. Uncrosslinked regions were dissolved by submerging the wafers in propylene glycol methyl ether acetate, followed by isopropyl alcohol, and then dried. PDMS (Sylgard 184, Dow Corning, MI, USA) was poured over the wafer and then degassed in a vacuum desiccator. After curing, the patterned PDMS was peeled off the surface and cut to be used as stamps (ESI Fig. S25†).

Micropatterning fibronectin on PDMS substrates

PDMS stamps were sonicated in a 70% EtOH bath for a minimum of 15 minutes and dried with compressed air under a sterile hood. The stamps were coated with 50 μg mL^{-1} fibronectin (Sigma-Aldrich, MO, USA) for a minimum of 45 minutes prior to patterning. Prior to this step, PDMS-coated 18 mm diameter circular glass coverslips were prepared by spin-coating with Sylgard 184 PDMS, which was cured overnight in a 65 °C oven, and then pre-treated in a UV-ozone cleaner (Jelight, CA, USA) for surface activation right before stamping. After fibronectin incubation, the stamps were gently dried with compressed air and placed onto the UVO-treated coverslips to transfer fibronectin in the desired pattern. Following pattern transfer, the coverslips were immersed in 1% Pluronic F127 (Sigma, MO, USA) for a minimum of 5 minutes to block cell adhesion to unpatterned areas, then rinsed three times with phosphate buffered saline (PBS). The patterned coverslips were stored in PBS at 4 °C until cell seeding.

Endothelial cell culture

Human umbilical vein endothelial cells (Lonza, HUVECs) were used for all the *in vitro* studies discussed in this study. HUVEC culture was maintained under sterile conditions, at 37 °C and 5% CO_2, using Medium 200 (Gibco, MA, USA) with the corresponding low serum endothelial growth supplement (Thermo Fisher Scientific, MA, USA). This medium supplement contains fetal bovine serum (2% v/v), hydrocortisone (1 μg ml^{-1}), human epidermal growth factor (10 ng ml^{-1}) basic fibroblast growth factor (3 ng ml^{-1}) and heparin (10 μg ml^{-1}). All cells used were between passage four to eight, with media exchange after 24 hours of seeding and every 48 hours thereafter. The micropatterned coverslips, with ~3600 FN islands per cm^2, were placed in a standard 12-well plate and seeded with HUVECs at a density of ~5300 cells per cm^2. The cells were allowed to adhere to the fibronectin pattern, and the medium was supplemented with 2.5 μM 8-CPT-cAMP (Abcam, MA, USA) between 24 to 72 hours after seeding to ensure compete adherens junction formation.

ENM synthesis and characterization

The ENMs used in our experiments were procured, synthesized, and characterized by Engineered Nanomaterials

Coordination Core (ERCC)—part of Nanotechnology Health Implications Research (NHIR) Consortium at Harvard School of Public Health. Detailed synthesis and characterization of the ENMs used in this study have been described elsewhere: citrate capped-capped Au and Ag NPs have been presented by Konduru *et al.*[79] and Ahn *et al.*,[36] respectively; SiO_2, Fe_2O_3, and Al_2O_3 ENMs have been presented by Beltran-Huarac *et al.*;[80] CNC and CNF have been presented by Pyrgiotakis *et al.*[81] The following ENMs were commercially available: TiO_2 were purchased by Acros Organics and have been previously characterized by Ahn *et al.*;[36] CuO and ZnO were purchased from Sigma Aldrich and Meliorum Technologies, respectively. The characterization data for CuO and ZnO are presented in ESI Fig. S26 and Tables S1, S2.†

ENM dispersion preparation

The dispersion preparation and colloidal characterization were conducted according to literature procedures.[82–84] We used an ultrasonic processor/sonic dismembrator (FB-505, Fisher Scientific, USA) calibrated according to a literature protocol,[85] which was found to deliver an acoustic power of 2.51 J s^{-1}. Each ENM stock solution was prepared with DNase/RNase free distilled water (Invitrogen, MA, USA) at a concentration of 500 μg ml^{-1}. To determine the minimum amount of sonication time for fully dispersing TiO_2, ZnO, SiO_2, CuO, Fe_2O_3 and Al_2O_3 in water, the critical delivered sonication energy (DSE_{cr}) was first calculated for each ENM type according to a literature procedure.[86] The DSE_{cr} of a specific ENM is defined as the DSE (in J mL^{-1}) required to achieve a solution with the lowest particle agglomeration state in DI H_2O. A 1 mL solution from the stock was used to measure the hydrodynamic diameter (dH) using dynamic light scattering (DLS; Malvern Nanosizer, Worcestershire, UK). The solution was sonicated for 1 min, vortexed for 10 s, and measured again. The process was continued until the dH and polydispersity index (PDI) values were not changing significantly (±5%).

All stock suspensions for the 6 ENMs mentioned above were then prepared in water according to their respective DSE_{cr} values. The DSE_{cr} for these ENMs are as follows: TiO_2 = 380 J mL^{-1}; ZnO = 420 J mL^{-1}; SiO_2 = 161 J mL^{-1}; CuO = 271 J mL^{-1}; Fe_2O_3 = 320 J mL^{-1}; Al_2O_3 = 388.5 J mL^{-1}. The working solutions (10 to 100 μg mL^{-1}) for these ENMs were prepared by diluting the sonicated 500 μg mL^{-1} stock solutions with HUVEC culture medium. For Au and Ag NPs, the supplied colloidal solutions were concentrated to 1200 μg mL^{-1} by using ultracentrifugation at 13 000 RPM for 20 min at 4 °C, which was then re-dispered in water, vortexed for 30 s, and then diluted to the final working concentrations with HUVEC cell culture media. For the nanocellulose polymorphs (CNC and CNF), a 1 mg mL^{-1} stock solution was first prepared in water and then vortexed at a high speed for 30 s seconds to ensure dispersion. The nanocellulose stock solutions were diluted with HUVEC cell culture media to the desired final concentrations. The DLS profiles for the stock solutions in water and ENM dispersions in cell culture media, except for CNC and CNF that have higher aspect ratios, are presented in the ESI Fig. S27.†

ENM exposure studies

After 24 h in normal culture and 24 h with cAMP-supplemented media, HUVEC pairs were treated with ENMs at varying concentrations for another 24 h (Fig. 1d). For HUVEC monolayers, ENM suspension on cAMP-supplemented culture media was introduced to the apical side of the well for 24 h. All ENM exposure experiments with HUVEC pairs and monolayers were performed three times. For the studies with ENM-induced cytoskeletal reorganization, cell pairs treated with calpeptin (Rho activator I, Cytoskeleton, Inc.; working concentration = 1 unit per mL) and Y-27632 (ROCK inhibitor, EMD Millipore; working concentration = 10 μM) were used as additional control groups. Exposure time for both drugs is 30 minutes as per the manufacturer's protocol to achieve maximum effect on actin fibers.

Permeability assay

HUVECs were seeded at a density of ~15 000 cells per cm^2 on Transwell® polyester membrane cell culture inserts (6.5 mm, 0.4 μm pore size, 0.33 cm^2 surface area; Corning, NY, USA). Prior to seeding, each insert was coated with 50 μg mL^{-1} of fibronectin for at least an hour at room temperature. The cells were cultured for 48 hours to allow for confluence prior to permeability measurements. We followed a previously-reported protocol[87] for calculating the macromolecular permeability of two representative fluorophores, Alexa Fluor 555 (400 Da; Invitrogen, MA, USA) and Oregon Green 488 (1.2 kDa; Thermo Fisher Scientific, MA, USA), across the HUVEC monolayers after 24 h of exposure to ENMs. Permeability measurements were also taken before exposure to ENMs to ensure that all monolayers have statistically similar permeability measurements prior to ENM exposure.

Cytotoxicity measurements

To measure ENM-induced changes in cellular viability, commercially-available assay kits were used for detecting the release of lactate dehydrogenase (LDH; Promega, WI, USA) and mitochondrial reductase activity using 3-(4,5-dimethylthiazol-2-yl)-5-(3-carboxymethoxyphenyl)-2-(4-sulfophenyl)-2*H*-tetrazolium (MTS; Abcam, MA, USA). For these tests, unpatterned HUVECs were seeded on 96-well plates at a density of ~15 600 cells per cm^2. For the LDH assay, cell culture media were collected from each sample in triplicate and then incubated with the reagents from the LDH assay kit. The absorbance of the resulting solution at 490 nm was recorded using a plate reader (Synergy HT; BioTek, NJ, USA). Similarly, the MTS assay was executed according to manufacturer's protocol, whereby the absorption of test solutions was also recorded at 490 nm. To establish the correct baseline per reading, the background signal at 650 nm and from each ENM suspension on fresh culture media at 490 nm were subtracted from the recorded absorbance values.

Immunostaining

Cells were fixed in 4% paraformaldehyde (PFA) for 10 min, followed by permeabilization with 0.05% Triton-X for another

15 min. Non-specific binding was prevented by blocking with a 5% bovine serum albumin (BSA) solution in PBS for 1 h. After these steps, the samples were incubated with primary antibodies against vinculin (1 : 500; Abcam, MA, USA), VE-cadherin (1 : 500; Abcam, MA, USA), or fibronectin (1 : 500; Sigma, MO, USA) for 2 h at room temperature, followed by incubation with the appropriate secondary antibodies (against rabbit IgG (H + L) conjugated to Alexa Fluor 488 or mouse IgG conjugated to Alexa Fluor 633; 1 : 200; Life Technologies, CA, USA) and Alexa Fluor 546 Phalloidin (1 : 200; Life Technologies, CA, USA) for 1 h at room temperature. To stain for nuclei, samples were incubated with 4′,6-diamidino-2-phenylindole dihydrochloride (DAPI; Invitrogen, CA, USA) solution with a working concentration of at least 300 nM for 5 minutes. The samples were washed at least three times with 0.5% BSA solution in between steps. After the last staining step, all samples were washed with PBS for at least three times and then mounted on a glass slide with Prolong Gold anti-fade agent (Life Technologies, CA, USA).

Cellular proliferation measurements

Proliferation of HUVECs with or without ENM treatment were assessed by immunostaining against a Ki67 antibody as the proliferation marker (1 : 500, Thermo Fisher Scientific, MA, USA; against rabbit IgG (H + L) conjugated to Alexa Fluor 488) and DAPI for counting the total number of cells. The standard immunostaining protocol described above was followed. For this measurement, unpatterned cells were seeded on 24-well plates at a density of ~5300 cells per cm^2. The % of Ki67-positive cells per number of DAPI-positive cells were calculated and averaged from two independent experiments with 3 wells per treatment condition (least 4 fields of view per well).

Darkfield microscopy

ENM localization was observed using the darkfield mode of an integrated hyperspectral and Raman microscope (CytoViva, AL, USA/Horiba, CA, USA). The corresponding darkfield images were obtained using a halogen lamp with aluminum reflector (Part L1090; International Light Technologies, MA, USA). All test samples with HUVEC pairs were fixed with 4% paraformaldehyde prior to mounting onto a glass slide with PBS.

Confocal microscopy and data analysis

All immunofluorescence images were acquired using a spinning disk confocal microscope (Olympus ix83, Andor spinning disk). Image analysis was conducted using Fiji, a distribution of ImageJ focused on biological image analysis.[88] Further details on image analysis, quantification of cell pair features and calculation of similarity index can be found in the ESI.† Custom ImageJ macros used for image analysis are available from the authors upon request. All data shown are mean ± standard error of the mean (SEM). Pearson product-moment correlation coefficient was calculated between the cellular architecture measurements and tissue permeability values reported in Fig. 8. Statistical significance was determined using a two-tailed Student's *t*-test (*$p < 0.05$, **$p < 0.005$, #$p < 0.001$).

Conflicts of interest

There are no conflicts to declare.

Acknowledgements

Research reported in this publication was supported by National Institute of Environmental Health Sciences of the National Institutes of Health under award numbers U01ES027272 and U24ES026946 as part of the Nanotechnology Health Implications Research (NHIR) Consortium. The content is solely the responsibility of the authors and does not necessarily represent the official views of the National Institutes of Health. The engineered nanomaterials used in the research presented in this publication have been procured or synthesized and characterized by the Engineered Nanomaterials Resource and Coordination Core (ERCC) at the Center for Nanotechnology and Nanotoxicology at Harvard School of Public Health, part of the NIEHS/NHIR consortium. This work was partially supported by the Wyss Institute for Biologically Inspired Engineering at Harvard University. Soft lithography work and darkfield imaging were performed at the Harvard Center for Nanoscale Systems (CNS), which is a member of the National Nanotechnology Infrastructure Network (NNIN) under NSF Award No. 1541959. The micropatterning experiments were performed in part at the Harvard MRSEC (Grant No. DMR-1420570). F. E. thanks the Amgen Foundation for summer fellowship support. H. A. M. A. would like to thank the American Chemical Society for generous support through the Irving S. Sigal Postdoctoral Fellowship. J. F. Z. acknowledges support from Harvard University and by the Organ Design and Engineering Postdoctoral Training (ODET) program through Brigham and Women's Hospital, National Institute of Biomedical Imaging and Bioengineering (NIBIB) and the National Institute of Health (Award No. 5-T32-EB016652-04). B.B.O. acknowledges support from the NIH Eunice Kennedy Shriver National Institute of Child Health and Human Development (Award No. F31-HD095594). The authors thank to Dr Sean P. Sheehy for providing the software used for similarity index measurements and Michael Rosnach for graphical assistance.

References

1 D. N. Granger and E. Senchenkova, Chapter 10, Endothelial Barrier Dysfunction, in *Inflammation and the Microcirculation*, Morgan & Claypool Life Sciences, San Rafael (CA), 2010.
2 S. M. Opal and T. Poll, *J. Intern. Med.*, 2014, **277**, 277–293.
3 M. E. Vance, T. Kuiken, E. P. Vejerano, S. P. McGinnis, M. F. Hochella Jr., D. Rejeski and M. S. Hull, *Beilstein J. Nanotechnol.*, 2015, **6**, 1769–1780.
4 Y. Cao, in *Cellular and Molecular Toxicology of Nanoparticles*, ed. Q. Saquib, M. Faisal, A. A. Al-Khedhairy

and A. A. Alatar, Springer International Publishing, Cham, 2018, pp. 59–69, DOI: 10.1007/978-3-319-72041-8_4.
5 J. D. Sisler, S. V. Pirela, S. Friend, M. Farcas, D. Schwegler-Berry, A. Shvedova, V. Castranova, P. Demokritou and Y. Qian, *Nanotoxicology*, 2015, **9**, 769–779.
6 Y. Zhang and W. X. Yang, *Beilstein J. Nanotechnol.*, 2016, **7**, 675–684.
7 P. L. Apopa, Y. Qian, R. Shao, N. L. Guo, D. Schwegler-Berry, M. Pacurari, D. Porter, X. Shi, V. Vallyathan, V. Castranova and D. C. Flynn, *Part. Fibre Toxicol.*, 2009, **6**, 1.
8 K. Buyukhatipoglu and A. M. Clyne, *J. Biomed. Mater. Res., Part A*, 2010, **96A**, 186–195.
9 Y. Liu, N. Rogel, K. Harada, L. Jarett, C. H. Maiorana, G. K. German, G. J. Mahler and A. L. Doiron, *Nanotoxicology*, 2017, **11**, 846–856.
10 E. Paszek, J. Czyz, O. Woznicka, D. Jakubiak, J. Wojnarowicz, W. Lojkowski and E. Stepien, *J. Biomed. Nanotechnol.*, 2012, **8**, 957–967.
11 M. I. Setyawati, C. Y. Tay, S. L. Chia, S. L. Goh, W. Fang, M. J. Neo, H. C. Chong, S. M. Tan, S. C. J. Loo, K. W. Ng, J. P. Xie, C. N. Ong, N. S. Tan and D. T. Leong, *Nat. Commun.*, 2013, **4**, 1673.
12 C. Y. Tay, P. Cai, M. I. Setyawati, W. Fang, L. P. Tan, C. H. L. Hong, X. Chen and D. T. Leong, *Nano Lett.*, 2014, **14**, 83–88.
13 R. Singhvi, A. Kumar, G. P. Lopez, G. N. Stephanopoulos, D. I. C. Wang, G. M. Whitesides and D. E. Ingber, *Science*, 1994, **264**, 696–698.
14 C. S. Chen, M. Mrksich, S. Huang, G. M. Whitesides and D. E. Ingber, *Science*, 1997, **276**, 1425.
15 M. Mrksich and G. M. Whitesides, *Trends Biotechnol.*, 1995, **13**, 228–235.
16 S. Alom Ruiz and C. S. Chen, *Soft Matter*, 2007, **3**, 168–177.
17 A. Quist, E. Pavlovic and S. Oscarsson, *Recent advances in microcontact printing*, 2005.
18 P. Leduc, E. Ostuni, G. Whitesides and D. Ingber, *Use of micropatterned adhesive surfaces for control of cell behavior*, 2002.
19 N. F. Huang, E. S. Lai, A. J. Ribeiro, S. Pan, B. L. Pruitt, G. G. Fuller and J. P. Cooke, *Biomaterials*, 2013, **34**, 2928–2937.
20 Q. Tseng, E. Duchemin-Pelletier, A. Deshiere, M. Balland, H. Guillou, O. Filhol and M. Théry, *Proc. Natl. Acad. Sci. U. S. A.*, 2012, **109**, 1506.
21 B. Sarker, C. Walter and A. Pathak, *ACS Biomater. Sci. Eng.*, 2018, **4**, 2340–2349.
22 J. Y. Sim, J. Moeller, K. C. Hart, D. Ramallo, V. Vogel, A. R. Dunn, W. J. Nelson and B. L. Pruitt, *Mol. Biol. Cell*, 2015, **26**, 2456–2465.
23 M. L. McCain, T. Desplantez, N. A. Geisse, B. Rothen-Rutishauser, H. Oberer, K. K. Parker and A. G. Kleber, *Am. J. Physiol.: Heart Circ. Physiol.*, 2012, **302**, H443–H450.
24 L. C. McSpadden, H. Nguyen and N. Bursac, *Circ.: Arrhythmia Electrophysiol.*, 2012, **5**, 821–830.
25 D. M. Pedrotty, R. Y. Klinger, N. Badie, S. Hinds, A. Kardashian and N. Bursac, *Am. J. Physiol.: Heart Circ. Physiol.*, 2008, **295**, H390–H400.
26 C. Brangwynne, K. K. Parker, S. Huang and D. E. Ingber, *In Vitro Cell. Dev. Biol.: Anim.*, 2000, **36**, 563–565.
27 J. L. Charest, J. M. Jennings, W. P. King, A. P. Kowalczyk and A. J. García, *J. Invest. Dermatol.*, 2009, **129**, 564–572.
28 D. E. Ingber, *Proc. Natl. Acad. Sci. U. S. A.*, 1990, **87**, 3579–3583.
29 S. Huang and D. E. Ingber, *Nat. Cell Biol.*, 1999, **1**, E131–E138.
30 A. M. Malek and S. Izumo, *J. Cell Sci.*, 1996, **109**, 713.
31 Z. Liu, J. L. Tan, D. M. Cohen, M. T. Yang, N. J. Sniadecki, S. A. Ruiz, C. M. Nelson and C. S. Chen, *Proc. Natl. Acad. Sci. U. S. A.*, 2010, **107**, 9944.
32 M. R. Ng, A. Besser, J. S. Brugge and G. Danuser, *eLife*, 2014, **3**, e03282.
33 C. S. Chen, M. Mrksich, S. Huang, G. M. Whitesides and D. E. Ingber, *Biotechnol. Prog.*, 2008, **14**, 356–363.
34 K. K. Parker, A. L. Brock, C. Brangwynne, R. J. Mannix, N. Wang, E. Ostuni, N. A. Geisse, J. C. Adams, G. M. Whitesides and D. E. Ingber, *FASEB J.*, 2002, **16**, 1195–1204.
35 D. E. J. Anderson and M. T. Hinds, *Ann. Biomed. Eng.*, 2011, **39**, 2329.
36 S. Ahn, H. A. M. Ardoña, J. U. Lind, F. Eweje, S. L. Kim, G. M. Gonzalez, Q. Liu, J. F. Zimmerman, G. Pyrgiotakis, Z. Zhang, J. Beltran-Huarac, P. Carpinone, B. M. Moudgil, P. Demokritou and K. K. Parker, *Anal. Bioanal. Chem.*, 2018, **410**, 6141–6154.
37 A. Nel, T. Xia, L. Madler and N. Li, *Science*, 2006, **311**, 622–627.
38 F. Peng, M. I. Setyawati, J. K. Tee, X. Ding, J. Wang, M. E. Nga, H. K. Ho and D. T. Leong, *Nat. Nanotechnol.*, 2019, **14**, 279–286.
39 M. I. Setyawati, C. Y. Tay and D. T. Leong, *Nanomedicine*, 2014, **9**, 1591–1594.
40 A. E. Nel, L. Madler, D. Velegol, T. Xia, E. M. Hoek, P. Somasundaran, F. Klaessig, V. Castranova and M. Thompson, *Nat. Mater.*, 2009, **8**, 543–557.
41 C. Y. Tay, M. I. Setyawati and D. T. Leong, *ACS Nano*, 2017, **11**, 2764–2772.
42 C. Endes, S. Camarero-Espinosa, S. Mueller, E. J. Foster, A. Petri-Fink, B. Rothen-Rutishauser, C. Weder and M. J. Clift, *J. Nanobiotechnol.*, 2016, **14**, 78.
43 M. Liu, Q. Li, L. Liang, J. Li, K. Wang, J. Li, M. Lv, N. Chen, H. Song, J. Lee, J. Shi, L. Wang, R. Lal and C. Fan, *Nat. Commun.*, 2017, **8**, 15646.
44 S. K. Lai, K. Hida, S. T. Man, C. Chen, C. Machamer, T. A. Schroer and J. Hanes, *Biomaterials*, 2007, **28**, 2876–2884.
45 C. Dalal, A. Saha and N. R. Jana, *J. Phys. Chem. C*, 2016, **120**, 6778–6786.
46 J. Zimmerman, H. A. M. Ardoña, G. Pyrgiotakis, J. Dong, B. M. Moudgil, P. Demokritou and K. K. Parker, *Nano Lett.*, 2019, **19**, 793–804.
47 D. Mohr, S. Frey, T. Fischer, T. Güttler and D. Görlich, *EMBO J.*, 2009, **28**, 2541.

48 J. F. Zimmerman, R. Parameswaran, G. Murray, Y. Wang, M. Burke and B. Tian, *Sci. Adv.*, 2016, **2**, e1601039.
49 S. Sukriti, M. Tauseef, P. Yazbeck and D. Mehta, *Pulm. Circ.*, 2014, **4**, 535–551.
50 G. E. Davis and D. R. Senger, *Circ. Res.*, 2005, **97**, 1093–1107.
51 N. Rogel, K. Harada, L. Jarett, C. H. Maiorana, G. K. German, G. J. Mahler and A. L. Doiron, *Nanotoxicology*, 2017, **11**, 846–856.
52 N. Prasain and T. Stevens, *Microvasc. Res.*, 2009, **77**, 53–63.
53 Y. Komarova and A. B. Malik, *Annu. Rev. Physiol.*, 2010, **72**, 463–493.
54 I. Singh, N. Knezevic, G. U. Ahmmed, V. Kini, A. B. Malik and D. Mehta, *J. Biol. Chem.*, 2007, **282**, 7833–7843.
55 K. Burridge and E. S. Wittchen, *J. Cell Biol.*, 2013, **200**, 9.
56 D. L. Huang, N. A. Bax, C. D. Buckley, W. I. Weis and A. R. Dunn, *Science*, 2017, **357**, 703.
57 J. L. Bays and K. A. DeMali, *Cell. Mol. Life Sci.*, 2017, **74**, 2999–3009.
58 N. M. Ramdas and G. V. Shivashankar, *J. Mol. Biol.*, 2015, **427**, 695–706.
59 D. A. Starr and H. N. Fridolfsson, *Annu. Rev. Cell Dev. Biol.*, 2010, **26**, 421–444.
60 A. J. Maniotis, C. S. Chen and D. E. Ingber, *Proc. Natl. Acad. Sci. U. S. A.*, 1997, **94**, 849.
61 J.-K. Kim, A. Louhghalam, G. Lee, B. W. Schafer, D. Wirtz and D.-H. Kim, *Nat. Commun.*, 2017, **8**, 2123.
62 M. Versaevel, T. Grevesse and S. Gabriele, *Nat. Commun.*, 2012, **3**, 671.
63 M.-A. P. Bray, W. J. Adams, N. A. Geisse, A. W. Feinberg, S. P. Sheehy and K. K. Parker, *Biomaterials*, 2010, **31**, 5143–5150.
64 S. Huveneers, J. Oldenburg, E. Spanjaard, G. van der Krogt, I. Grigoriev, A. Akhmanova, H. Rehmann and J. de Rooij, *J. Cell Biol.*, 2012, **196**, 641.
65 J. Millán, R. J. Cain, N. Reglero-Real, C. Bigarella, B. Marcos-Ramiro, L. Fernández-Martín, I. Correas and A. J. Ridley, *BMC Biol.*, 2010, **8**, 11.
66 M. Desouza, P. W. Gunning and J. R. Stehn, *Bioarchitecture*, 2012, **2**, 75–87.
67 S. Povea-Cabello, M. Oropesa-Ávila, P. de la Cruz-Ojeda, M. Villanueva-Paz, M. de la Mata, M. J. Suárez-Rivero, M. Álvarez-Córdoba, I. Villalón-García, D. Cotán, P. Ybot-González and A. J. Sánchez-Alcázar, *Int. J. Mol. Sci.*, 2017, **18**, 2393.
68 C. D. Buckley, J. Tan, K. L. Anderson, D. Hanein, N. Volkmann, W. I. Weis, W. J. Nelson and A. R. Dunn, *Science*, 2014, **346**, 1254211.
69 M. Giannotta, M. Trani and E. Dejana, *Dev. Cell*, 2013, **26**, 441–454.
70 E. Dejana and F. Orsenigo, *J. Cell Sci.*, 2013, **126**, 2545.
71 M. Galisteo, M. Sánchez, R. O. Vera, M. González, A. Anguera, J. Duarte and A. Zarzuelo, *J. Nutr.*, 2005, **135**, 2399–2404.
72 H. Guo, J. Zhang, M. Boudreau, J. Meng, J.-J. Yin, J. Liu and H. Xu, *Part. Fibre Toxicol.*, 2016, **13**, 21.
73 X. Sun, J. Shi, X. Zou, C. Wang, Y. Yang and H. Zhang, *J. Hazard. Mater.*, 2016, **317**, 570–578.
74 C. Cerutti and A. J. Ridley, *Exp. Cell Res.*, 2017, **358**, 31–38.
75 A. P. Adam, *Mediators Inflammation*, 2015, **2015**, 24.
76 S. Dong, A. A. Hirani, K. R. Colacino, Y. W. Lee and M. Roman, *Nano LIFE*, 2012, **02**, 1241006.
77 D. Kugelmann, L. T. Rotkopf, M. Y. Radeva, A. Garcia-Ponce, E. Walter and J. Waschke, *Sci. Rep.*, 2018, **8**, 13229.
78 S. Ahn, H. A. M. Ardoña, P. H. Campbell, G. M. Gonzalez and K. K. Parker, *ACS Appl. Mater. Interfaces*, 2019, **11**, 33535–33547.
79 N. V. Konduru, R. M. Molina, A. Swami, F. Damiani, G. Pyrgiotakis, P. Lin, P. Andreozzi, T. C. Donaghey, P. Demokritou, S. Krol, W. Kreyling and J. D. Brain, *Part. Fibre Toxicol.*, 2017, **14**, 42.
80 J. Beltran-Huarac, Z. Zhang, G. Pyrgiotakis, G. DeLoid, N. Vaze, S. M. Hussain and P. Demokritou, *NanoImpact*, 2018, **10**, 26–37.
81 G. Pyrgiotakis, W. Luu, Z. Zhang, N. Vaze, G. DeLoid, L. Rubio, W. A. C. Graham, D. C. Bell, D. Bousfield and P. Demokritou, *Cellulose*, 2018, **25**, 2303–2319.
82 G. DeLoid, J. M. Cohen, T. Darrah, R. Derk, L. Rojanasakul, G. Pyrgiotakis, W. Wohlleben and P. Demokritou, *Nat. Commun.*, 2014, **5**, 3514.
83 G. M. DeLoid, J. M. Cohen, G. Pyrgiotakis and P. Demokritou, *Nat. Protoc.*, 2017, **12**, 355–371.
84 G. M. DeLoid, J. M. Cohen, G. Pyrgiotakis, S. V. Pirela, A. Pal, J. Liu, J. Srebric and P. Demokritou, *Part. Fibre Toxicol.*, 2015, **12**, 32.
85 J. S. Taurozzi, V. A. Hackley and M. R. Wiesner, *Nanotoxicology*, 2011, **5**, 711–729.
86 J. Cohen, G. Deloid, G. Pyrgiotakis and P. Demokritou, *Nanotoxicology*, 2013, **7**, 417–431.
87 I. Bischoff, M. C. Hornburger, B. A. Mayer, A. Beyerle, J. Wegener and R. Fürst, *Sci. Rep.*, 2016, **6**, 23671.
88 J. Schindelin, I. Arganda-Carreras, E. Frise, V. Kaynig, M. Longair, T. Pietzsch, S. Preibisch, C. Rueden, S. Saalfeld, B. Schmid, J.-Y. Tinevez, D. J. White, V. Hartenstein, K. Eliceiri, P. Tomancak and A. Cardona, *Nat. Methods*, 2012, **9**, 676.

